Journal of Power Sources 194 (2009) 104–111

Contents lists available at ScienceDirect

Journal of Power Sources

journal homepage: www.elsevier.com/locate/jpowsour

Influence of Cr on structural and optical properties of TiO_2:Cr nanopowders prepared by flame spray synthesis

A. Trenczek-Zajac[a], M. Radecka[a,*], M. Jasinski[a], K.A. Michalow[a,d], M. Rekas[a], E. Kusior[b], K. Zakrzewska[b,c], A. Heel[d], T. Graule[d], K. Kowalski[e]

[a] Faculty of Materials Science and Ceramics, AGH University of Science and Technology, al. Mickiewicza 30, 30-059 Cracow, Poland
[b] Faculty of Electrical Engineering, Automatics, Computer Science and Electronics, AGH University of Science and Technology, al. Mickiewicza 30, 30-059 Cracow, Poland
[c] Laboratoire Kastler-Brossel, Université P. et M. Curie, 4, place Jussieu, 75 005 Paris, France
[d] EMPA, Swiss Federal Laboratories for Materials Testing and Research, Laboratory for High Performance Ceramics, Uberlandstrasse 129, 8600 Dubendorf, Switzerland
[e] Faculty of Metals Engineering and Industrial Computer Science, AGH University of Science and Technology, al. Mickiewicza 30, 30-059 Cracow, Poland

ARTICLE INFO

Article history:
Received 30 January 2009
Received in revised form 21 February 2009
Accepted 23 February 2009
Available online 6 March 2009

Keywords:
TiO_2
Nanopowders
Band gap
Photocatalysis

ABSTRACT

Influence of chromium incorporation on structural and optical properties of titanium dioxide nanopowders obtained by flame spray synthesis, FSS is studied by means of: X-ray diffraction, XRD; Raman spectroscopy; transmission electron spectroscopy, TEM; photoelectron spectroscopy, XPS and optical spectrophotometry over the ultraviolet, UV and visible range of the light spectrum from 250 nm to 2200 nm. The specific surface area, SSA, of the powders has been adjusted from 48 m^2/g for TiO_2 + 0.1 at.% Cr to 177 m^2/g for TiO_2 + 15 at.% Cr which is accompanied by a decrease in the anatase grain size from 21 nm to 5 nm. The anatase-to-rutile ratio changes with Cr^{3+} concentration but there is no evidence of precipitation of chromium oxides or chromium titanates. Incorporation of Cr^{3+} into TiO_2 lattice, as proved by XPS, is found to affect the electronic structure of TiO_2, as indicated by the optical spectrophotometry. The impurity band is formed within the forbidden band gap of titanium dioxide which results in the additional absorption within the visible range of the light spectrum. The general aim of this work is to improve the visible light absorption and hence the efficiency of photocatalytic decomposition of organic contaminants.

1. Introduction

Efficient degradation of organic contaminants by means of photocatalysis as well as generation of hydrogen through photoelectrochemical processes still necessitates an extensive work on devices actively performing under solar radiation. Titanium dioxide, TiO_2, the most widely accepted photocatalyst and photoanode, has excellent properties solely in the UV range of the light spectrum.

Utilization of solar radiation requires materials with sufficient light absorption within the visible range from λ=400 nm to λ=700 nm. The fundamental absorption edge of all polymorphic forms of TiO_2 occurs at $\lambda < 400$ nm, due to too large separation between the top of the valence band, VB, and the bottom of the conduction band, CB. To be specific, the forbidden band gap is 3.0 eV for rutile and 3.2 eV for anatase. Therefore, in order to benefit from all other remarkable features of TiO_2, e.g., stability and resistance to photocorrosion, the only solution is to modify TiO_2 absorption spectrum by either a shift towards longer wavelengths or by introducing additional absorption features within the visible range.

It is well known that a considerable shift of the absorption spectrum of TiO_2 towards visible spectrum can be reached by doping TiO_2 with certain transition metal ions such as Cr^{3+} [1–6]. However, incorporation of foreign species is usually accompanied by a substantial loss of the photocatalytic efficiency, the reason of which can be attributed to the increased recombination rate [5,7,8].

Therefore, in spite of the considerable effort in this domain, many controversial results concerning the effect of cation doping upon photocatalytic and photoelectrochemical efficiency have been reported [9]. Enhanced photoactivity has been obtained for Cr^{3+} [6,10]. However, studies also revealed that metal doping can result in thermal instability and increased carrier trapping [11,12].

There are many factors that influence the efficiency of photocatalytic processes in the case of TiO_2 doped with transition metals [13]. They include not only the type and level of doping but also:

- distribution of dopants,
- particle size of the host material,
- degree of crystallinity and relative amount of the polymorphic phases: anatase and rutile,

* Corresponding author. Tel.: +48 12 6172526; fax: +48 12 6172493.
E-mail address: radecka@agh.edu.pl (M. Radecka).

0378-7753/$ – see front matter © 2009 Elsevier B.V. All rights reserved.
doi:10.1016/j.jpowsour.2009.02.068

- surface properties of the photocatalyst (also in respect to adsorption of organics and dyes),
- type of the organic probe to be degraded.

Therefore, it is not surprising that the elaboration procedure and even the method of doping can affect the properties of the catalyst [3].

Among the factors acting on the photoactivity, the particle size and the degree of crystallinity have been considered as the most important [14]. Small particle size combined with a high degree of crystallinity have been found to enhance the photocatalytic activity in the case of TiO_2 nanopowders obtained by flame aerosol synthesis [14]. High specific surface area of nanopowders with an increased surface-to-volume ratio is expected to enhance the surface charge carrier transfer rate at the expense of recombination rate of electron–hole (e^-/h^+) pairs. As a consequence the quantum yield is improved for nanocrystalline photocatalysts.

However, the dependence of photoactivity on the particle size is by no means straightforward. Zhang et al. [15] have argued that, below a certain size limit, most of e^-/h^+ pairs are created close to the surface and undergo rapid surface recombination due to the abundant surface trapping sites.

We focused in the past [4,5,8] on titanium dioxide thin films and microcrystalline ceramics doped with transition metals such as chromium. In this paper we undertake a study on structural and optical properties of TiO_2 nanopowders with incorporated chromium for reasons outlined above.

Nanopowders of TiO_2 doped with transition metals can be prepared in many processes: wet impregnation [16,17], sol–gel [3], combination of sol–gel with hydrothermal treatment [6,18] and ion implantation [19]. Sol–gel leads to the greatest possible homogeneous distribution of dopants in the host matrix. Hydrothermal ion-intercalation was used for successful deposition of Cr-doped TiO_2 nanotubes with high photoefficiency over the visible range of the solar spectrum [10].

Here, we have used flame spray synthesis (FSS) as a method that allows to achieve crystalline powders in a single step thanks to high temperature in the flame [20]. The effect of chromium concentration on the phase composition, particle size and morphology is discussed. Particular attention is paid to the influence of chromium on the optical absorption of TiO_2 nanoparticles.

2. Experimental

2.1. Elaboration of powders

Nanopowders of TiO_2 and those of TiO_2:Cr were prepared by FSS. This method of powder elaboration along with the presentation of the FSS plant has been discussed in detail before [see for example [20,21]].

Titanium tetra-isopropoxide (TTIP, Ti $(C_3H_7O)_4$, 99%, VWR) and solution of chromium acetylacetonate (CHAA, $C_{15}H_{21}CrO_6$, 99%, ACROS) in m-xylene (1,3-dimethylobenzene, C_8H_{10}, 99.9% anhydrous, ACROS) were used as precursors of Ti and Cr, respectively. The precursors and m-xylene were further mixed in proportions required to reach the desired chromium concentration range (0.1–15 at.%) by application of the control over the flow rates of components of the precursor mixture. Then, the precursor mixture was atomized by a gas-assisted external nozzle and the resulting combustible aerosol was dispersed into fine droplets and oxidized in acetylene–oxygen flame. All gas flow rates were adjusted by mass flow controllers (Bronkhorst, HI-TEC, Netherlands). The representative powder particles were collected on glass fiber filters.

The composition, particle diameter and specific surface area (SSA) of the prepared powders were controlled by the flow rate of the precursors.

2.2. Measurement techniques

Particle size and SSA, are the most important parameters deciding about the performance of devices based on nanopowders. Therefore, in the first place, a careful characterization of elaborated materials was carried out.

The SSA of nanopowders was determined from nitrogen adsorption BET (Brunauer–Emmett–Teller) isotherms obtained with a Beckman–Coulter SA3100. Prior to measurements, surface adsorbed water has been removed by heating the powders for 2 h at 180 °C under nitrogen atmosphere.

X-ray diffraction XRD measurements were performed on X'Pert MPD Philips diffractometer within the range of diffraction angles 2θ from 10° to 80° with the Cu Kα filtered radiation. Crystallographic and phase analysis was carried out by means of an implemented program of line profile analysis, LPA. The degree of crystallinity, the contributions from anatase/rutile and amorphous phase, crystallite size and the lattice constants were calculated.

TEM images were recorded with a Philips CM30 operating at 300 kV. The primary particle size, shape and distribution of particles were of particular interest. The samples for TEM measurements were deposited onto carbon coated copper grids.

Complementary studies of the Raman effect were carried out. Raman spectra were obtained in the backscattering geometry using a Renishaw Ramascope 2000 with a spectral resolution of 1 cm^{-1}. The 632.8 nm line of the He–Ne laser was focused on the samples through 50× objective of the microscope, the power of laser power beam on the sample being 0.5 mW. Raman spectra were recorded at room temperature.

The chemical states of elements were investigated by an X-ray photoelectron spectroscopy (XPS) method using a VSW (Vacuum Systems Workshop Ltd.) instrument equipped with a concentric hemispherical (150 mm radius) electron analyzer and a two-plate 18-channel detector (Galileo). The electron spectrometer was operated at a fixed analyzer transmission (FAT) mode with a constant pass energy of 22 eV. The X-ray source was the Mg anode emitting the Kα (1253.6 eV) radiation of 200 W. Background pressure in the analytical chamber was 5×10^{-8} mbar. Calibration of the binding energy scale was done by assuming the position of the adventitious C 1s line at 284.6 eV.

Forbidden band gap of TiO_2 nanopowders and energies of optical transitions from the impurity band to the CB were derived from the optical spectra of diffuse reflectance $R_{Diff}(\lambda)$. The spectrophotometric measurements of $R_{Diff}(\lambda)$ were performed over the wavelength range 250–2200 nm with Perkin Elmer Lambda 19 double beam instrument equipped with a 150 mm integrating sphere. Kubelka–Munk model and analysis based on differential reflection spectra were used to determine independently the energies of the fundamental optical transitions.

3. Results and discussion

Table 1 recapitulates the most important results of our research pertaining to the morphology of nanopowders of undoped TiO_2 and those of TiO_2:Cr, prepared by FSS. The SSA changes from about 38 m^2/g for undoped TiO_2 and 48 m^2/g for TiO_2 to 0.1 at.% Cr to 177 m^2/g for TiO_2 + 15 at.% Cr. The most significant change in the SSA occurs between 1 at.% and 5 at.% of Cr. Assuming, that the powder is composed of uniform, nonporous and spherical grains of the diameter $2r_{avg}$, the BET-equivalent grain radius can be calculated from:

$$r_{avg} = \frac{3}{SSA \times (x_A \times d_A + x_R \times d_R + x_{am} \times d_{am})}$$

Table 1
Quantitative results of analysis of XRD diffraction patterns of Cr^{3+}-doped TiO_2 nanopowders; LPA is the acronym of Line Profile Analysis; SSA obtained from BET isotherms.

at.% Cr	Specific surface area SSA (m^2/g)	BET-equivalent grain diameter $2r_{avg}$ (nm)	Crystallite size from LPA of XRD (nm)		Lattice parameters (nm) anatase		Lattice parameters (nm) rutile		Weight percenage of rutile %	Fraction of amorphous phase
			anatase	rutile	a ±0.0001	c ±0.0003	a ±0.0001	c ±0.0001		
0	37.5	41.5	26.8	13.6	0.3784	0.9512	0.4606	0.2956	5.2	0.26
0.1	48.4	32.1	21.2	9.6	0.3785	0.9511	0.4598	0.2955	5.2	0.32
0.2	47.6	32.7	22.7	11.2	0.3785	0.9507	0.4597	0.2953	4.8	0.02
0.5	72.2	21.5	15.7	13.0	0.3784	0.9511	0.4597	0.2951	7.2	0.26
1	87.1	17.8	13.8	9.3	0.3786	0.9507	0.4595	0.2954	9.0	0.16
5	126.6	12.1	9.1	7.5	0.3781	0.9499	0.4596	0.2950	16.2	0.14
10	160.7	9.5	6.0	6.5	0.3779	0.9514	0.4595	0.2953	24.1	0.40
15	176.6	8.6	5.0	8.2	0.3780	0.9526	0.4590	0.2960	24.8	0.43

where the subscripts: A, *R* and *am* refer to anatase, rutile and amorphous phases, respectively; *x* denotes the volume ratio of each phase and d stands for density.

The increase in chromium concentration from 0.1 at.% to 15 at.% is accompanied by a decrease in the grain size from 32.1 nm to 8.6 nm, respectively, as determined from BET measurements of SSA. These values are higher than crystallite sizes determined from LPA of XRD studies (Table 1). This fact can be explained assuming that nanoparticles are composed of smaller crystallites.

X-ray diffraction patterns of nanopowders prepared by FSS are compared in Fig. 1. The XRD results show that both polymorphic forms of TiO_2, i.e., anatase and rutile, are present with anatase that dominates. The detailed phase analysis based on fitting the overall angular scan range from 22° to 42° presented in Fig. 2, indicates that the lowest weight percentage of rutile in undoped TiO_2 nanopowders amounts to 4–5%. The rutile-to-anatase ratio increases with the increasing Cr concentration as shown in Table 1 but at the same time the degree of crystallization of nanopowders diminishes, which is indicated by XRD peaks widening (contribution from the amorphous background becomes more significant). Neither chromium oxide nor chromium titanates were identified by XRD even at the highest concentration (15 at.% Cr) in spite of the fact that the solubility limit of Cr^{3+} in TiO_2 is less than 10 at.%. Similar effect has been observed before [3]. Furthermore, very small changes in the lattice parameters of rutile and anatase TiO_2 can be seen (Table 1). The lattice constants decrease with the increased Cr content up to 1 at.%. This change is more pronounced for '*a*' than for '*c*' and less evident for anatase than for rutile. However, this distortion of lattice is quite infinitesimal which may be due to the fact that Cr^{3+} and Ti^{4+} ions have nearly the same ionic radius, i.e., 0.0615 nm for Cr^{3+} and 0.0605 nm for Ti^{4+} [22].

Changes in the lattice parameters with dopant concentration described by Vegard's law are often treated as a proof for forma-

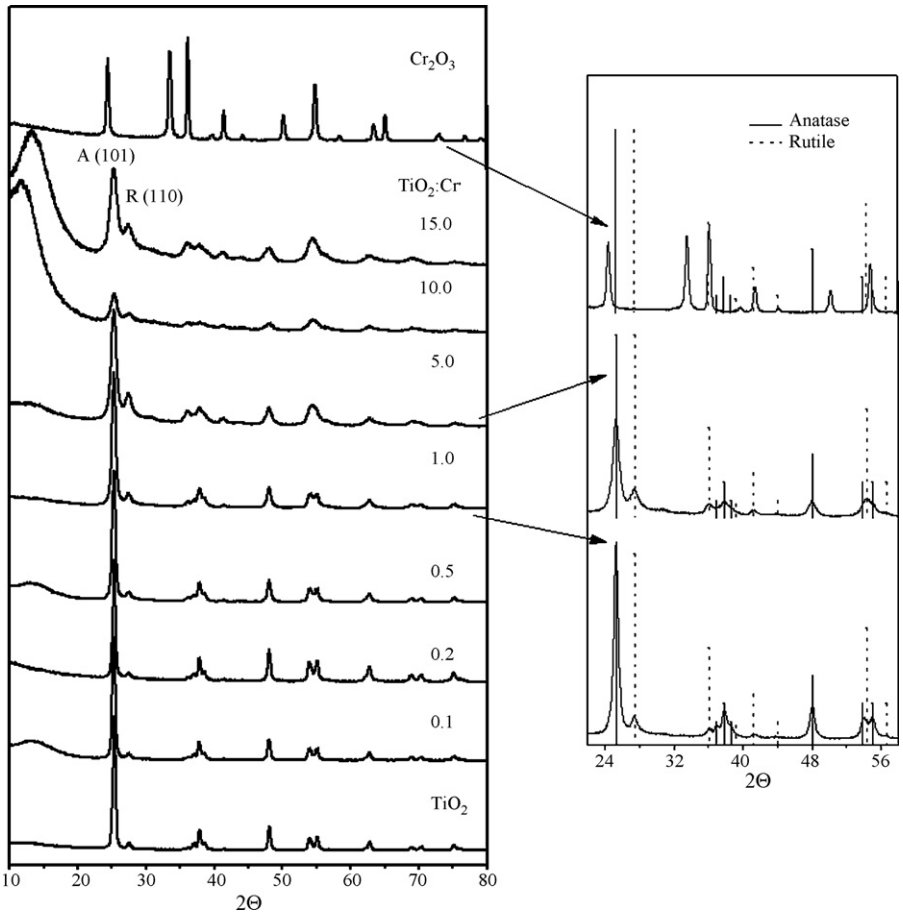

Fig. 1. X-ray diffraction patterns of TiO_2 and TiO_2:Cr nanopowders prepared by FSS. The pattern for Cr_2O_3 nanopowder with SSA = 32.4 m^2/g is given for comparison.

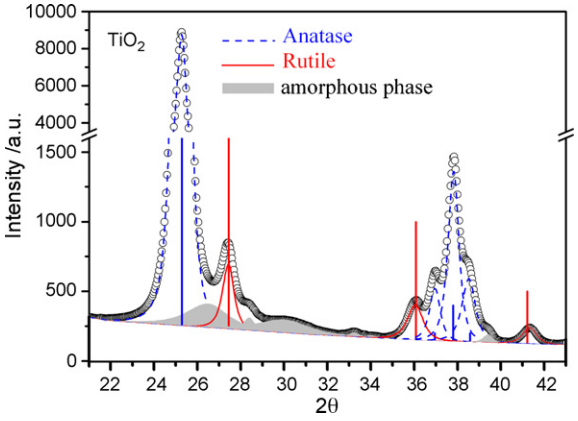

Fig. 2. The analysis of a typical XRD pattern of a TiO_2 nanopowder; determination of contributions from anatase, rutile and amorphous phase.

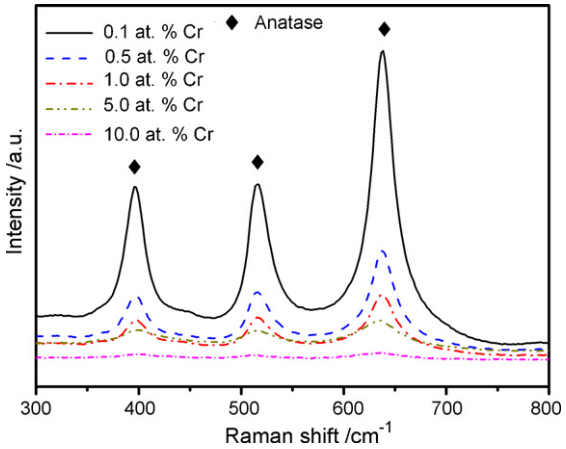

Fig. 3. Raman spectra of TiO_2:Cr nanopowders prepared by FSS.

tion of solid solutions. This is not the case of TiO_2 for the following reasons.

According to XRD results, the nanopowders are composed of three phases: anatase, rutile and amorphous one. This fact makes impossible the verification of the Vegard's law.

There are several reports [e.g., [23,24]] claiming that lower charge than Ti^{4+} may be compensated not only by oxygen vacancies V_O but also by titanium interstitial ions Ti_i. Thus, the substitutional incorporation of chromium into TiO_2 may be expressed, using the Kröger–Vink notation, as:

$$Cr_2O_3 \rightarrow 2Cr'_{Ti} + 3O_O + V_O^{\bullet\bullet} \quad (1)$$

$$2Cr_2O_3 + Ti_{Ti} \rightarrow 4Cr'_{Ti} + 6O_O + Ti_i^{4+} \quad (2)$$

both mechanisms given by Eqs. (1) and (2) show the opposite effects on the lattice parameter.

Gibb and Anderson [25] suggested the participation of incorporated chromium ions in formation of Anderson phases. There are no theoretical predictions about the effect of Anderson phases on the lattice parameters.

However, there are many other both direct and indirect proofs of substitutional incorporation of chromium in TiO_2. They include:

- thermodynamic studies and resulting phase diagrams [26,27],
- XRD studies [3,6,10,28],
- electrical and electrochemical studies [29–32],
- transport properties [33,34],
- XANES studies [10].

Complementary information on the crystallinity of nanopowders has been gained from the Raman effect. The characteristic peaks in Raman spectra of titanium dioxide depend on the crystallization and phase content. Three Raman-active fundamental modes of the anatase polymorphic modification of TiO_2 appear at 392 cm^{-1} (O—Ti—O bending type vibrations), 517 cm^{-1} and 635 cm^{-1} (Ti—O stretching type vibrations). As it is shown in Fig. 3 for TiO_2:Cr nanopowders obtained by flame spray synthesis, all three peaks are distinct at 0.1 at.% Cr. This remains in agreement with XRD results showing that at this concentration of chromium the powders are well-crystallized.

Small and wide feature extending between 440–460 cm^{-1} and a shoulder at 635 cm^{-1}–anatase peak indicates the presence of small amount of rutile with its Raman peaks at 455 cm^{-1} and 607 cm^{-1}. The quantitative contribution from rutile polymorphic form has been determined from XRD (see Table 1). Gradual amorphisation with the increase in Cr concentration is clearly indicated by a progressive disappearance of peaks in the Raman spectra.

TEM images (Fig. 4) from as-prepared flame-made titanium dioxide nanopowders show a typical particle morphology which can be expected from flame spray synthesis of metal–organic titanium precursors. The particles in the representative overviews are mainly spherical-shaped, non-aggregated and do not possess any interstitial particle necking, which is typical for such a kind of process under these conditions. High resolution imaging (Fig. 5) of the undoped TiO_2 revealed clearly the high crystallinity what can be seen from the lattice fringes within the primary particle structure and also from the well-defined XRD pattern. However, for 15 at.% Cr in TiO_2, lattice fringes are still visible but less obvious than in undoped TiO_2. This indicates clearly that some amorphous component is present. This amorphisation reflects also the observation made by amorphous content calculations of XRD data (Table 1).

With the increasing amount of chromium, the primary particle size is decreasing significantly. The reason for this is based on the fact that the Cr-content was realized by varying the flow rate of the Cr-acetylacetonate/m-xylene mixture, while the TTIP flow rate was kept constant. Hence, a dilution effect occurs by the increased amount of combustion products, what results in smaller particles. Such a dilution effect was demonstrated in [14] for undoped TiO_2 nanopowders.

Fig. 6 and Table 2 contain the results of XPS studies. The spectrum of Cr_2O_3 nanopowder prepared by FSS consists of a characteristic Cr $2p_{3/2}$ and Cr $2p_{1/2}$ doublet at the binding energies 575.9 eV and 586.0 eV, respectively. Additionally, the satellite peaks of Cr 2p appear at 565.8 eV and 567.6 eV. When Cr is incorporated into TiO_2, in spite of Cr 2p lines and their satellites, there is a single Ti 2s line in close proximity, i.e., at 565 eV. Moreover, the satellites of Ti 2s occur over the binding energy range where the principal Cr 2p peaks are located thus making the fitting more complicated. In the case of 0.2 at.% Cr, the peak intensity of Ti 2s satellites is even greater than that of principal components of Cr 2p. At 10 at.% Cr, the contribution from satellites is much smaller allowing for much more accurate identification of species.

The binding energies determined from XPS (Table 2) indicate that chromium is present as Cr^{3+} in TiO_2:Cr nanopowders. Small shift of Cr 2p doublet towards higher binding energies with the increasing chromium content suggests a charge transfer typical from Cr^{3+} to Cr^{4+} transition that accompanies substitutional incorporation of chromium for titanium. The difference $\Delta E_B = E_{Cr\ 2p3/2} - E_{Ti\ 2p3/2}$ between the binding energies of Cr $2p_{3/2}$ and Ti $2p_{3/2}$ peaks increases with the increased Cr content which remains consistent with this conclusion.

Transition metals may introduce large modifications in the electronic structure of the host material. This can be viewed as a

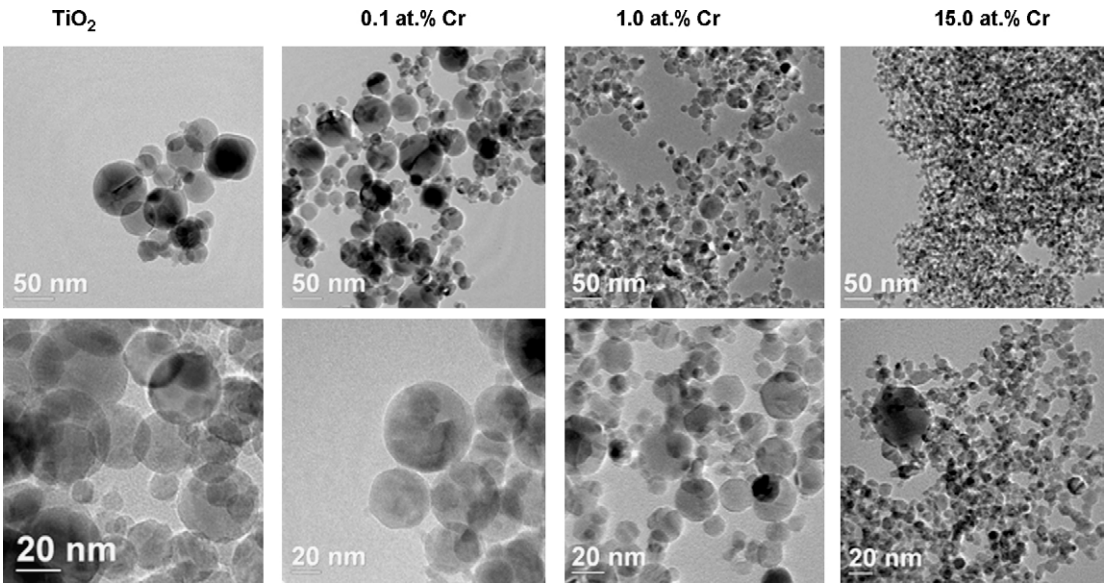

Fig. 4. TEM images of nanopowders prepared by FSS.

substantial change in the light absorption spectrum in the vicinity of the fundamental edge that results from electron transitions from the valence VB to the conduction band CB. Wilke and Breuer [3] observed the most dramatic shift in the photoacoustic absorption spectrum from 400 nm for undoped TiO_2 to 629 nm for 0.1 at.% Cr. This corresponds to an enormous change in energy of the electron transition, i.e., from 3.1 eV to 1.9 eV which seems somewhat unrealistic.

The optical diffuse reflectance spectra $R_{Diff}(\lambda)$ of nanopowders prepared by FSS are given in Fig. 7. The modifications in the $R_{Diff}(\lambda)$ are accompanied by changes in the color of powders from white for TiO_2, through yellow at intermediate doping level, up to dark green

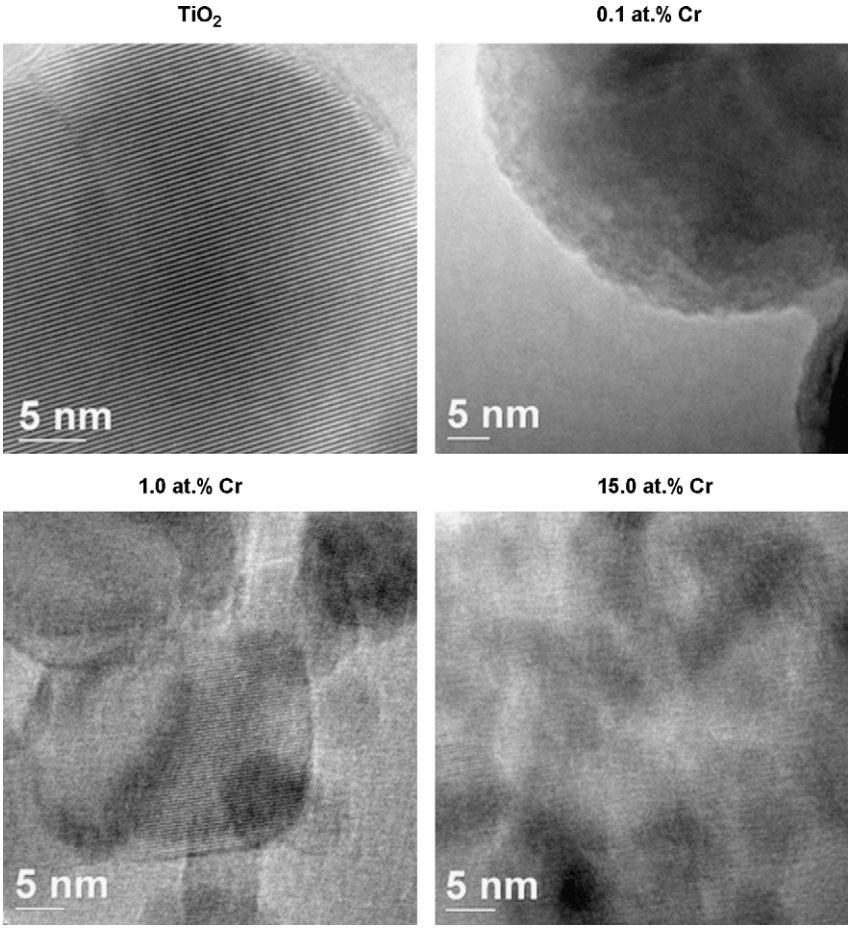

Fig. 5. HR TEM images of TiO_2 and TiO_2:Cr nanopowders.

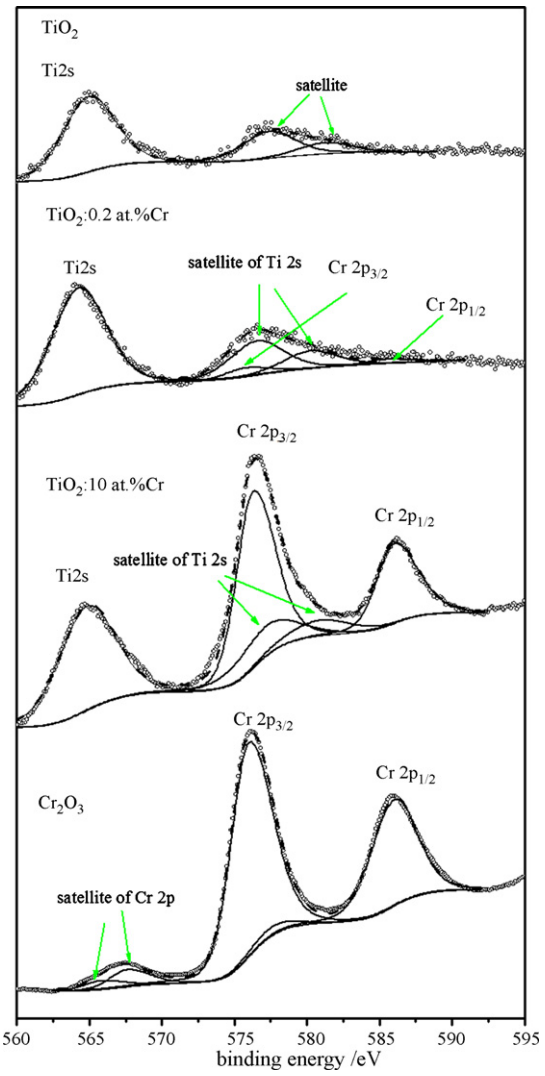

Fig. 6. XPS results for TiO_2 and TiO_2:Cr nanopowders prepared by FSS over the range of binding energy in which Cr 2p and Ti 2p lines occur. The XPS spectrum for Cr_2O_3 nanopowder with SSA = 32.4 m^2/g is given for comparison.

for the highest concentration of Cr^{3+} (15 at.%). Up to 1 at.% Cr, the reflectance spectra exhibit a well-pronounced fundamental absorption edge that manifest itself as an abrupt rise in the $R_{Diff}(\lambda)$ with the increasing wavelength. One should keep in mind, that the thickness (3 mm) of the powder sample, prepared for optical measurements, was large enough to avoid any transmission of light through it. The steepest fundamental absorption edge is seen for undoped TiO_2 nanopowder. This is not surprising as no defects are formed within the forbidden band gap of this material. The increased level of doping with Cr^{3+} results in an important perturbation in the region close to the fundamental edge and manifest itself as a decrease in

Table 2
Binding energies of Cr $2p_{3/2}$ and Ti $2p_{3/2}$ XPS peaks for TiO_2:Cr nanopowders.

	Binding energy (eV)		Binding energy shifts $\Delta E_B = E_{Cr\ 2p3/2} - E_{Ti\ 2p3/2}$ (eV)
	Cr $2p_{3/2}$	Ti $2p_{3/2}$	
TiO_2		458.5	
Cr_2O_3	575.9		
TiO_2:0.2 at.% Cr	575.6	458.0	117.6
TiO_2: 0.5at.% Cr	576.0	458.4	117.6
TiO_2: 5 at.% Cr	575.6	457.8	117.8
TiO_2: 10 at.% Cr	576.3	458.1	118.2

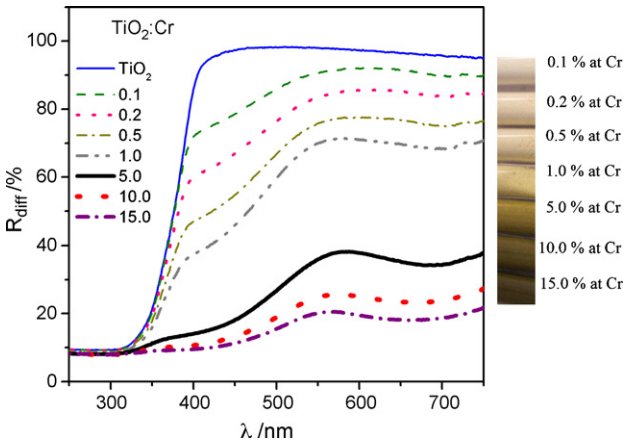

Fig. 7. Optical diffuse reflectance R_{Diff} as a function of wavelength λ for TiO_2 and TiO_2:Cr nanopowders prepared by FSS.

the $R_{Diff}(\lambda)$ for λ between 350 nm and 450 nm. However, the fundamental absorption edge is preserved up to 1 at.% Cr. The most dramatic change occurs between 1 at.% Cr and 5 at.% Cr which remains in agreement with XRD results. The fundamental absorption edge disappears while the absorption increases substantially within the visible range of the light spectrum, which is seen as a pronounced decrease in $R_{Diff}(\lambda)$.

The analysis of the reflectance spectrum $R_{Diff}(\lambda)$ was performed by two different methods: Kubelka–Munk model and analysis of differential reflection spectra. The maximum in differential reflectance $dR_{Diff}/d\lambda$ spectrum (Fig. 8) is very sensitive to optical transitions, the energy of which is determined by the wavelength at which $dR_{Diff}/d\lambda$ attains its maximum [35]. On the contrary, the Kubelka–Munk approach (Fig. 9) allows to determine the effective absorption [36] assuming that the scattering is independent of wavelength over this narrow wavelength range. Comparison between the values of photon energies of the optical transitions calculated from the analysis in Figs. 8 and 9 indicates that there is no much change between TiO_2 and TiO_2:0.1 at.% Cr. Two optical transitions of energies 3.33–3.35 eV and 3.17–3.19 eV are derived independently of the analysis method used (Fig. 8a and b and Fig. 9a and b) and might be attributed to the band gap of anatase and rutile, respectively (Table 3). Larger than typical values of E_g can be accounted for by the quantum size effect that leads to an increase in the band gap separation due to the decreased grain size [37]. With the increasing Cr content, the discrepancies between Kubelka–Munk model (Fig. 9c and d) and the analysis of maximum in the differential reflectance $dR_{Diff}/d\lambda$ become more profound (Fig. 8c and d). The highest transition energy of 3.42 eV obtained from the maximum in differential reflectance $dR_{Diff}/d\lambda$ (Table 3) cannot be fitted with the Kubelka–Munk model (Fig. 9c). However, when the doping level increases above 1 at.% Cr the energies of optical transitions are more difficult to calculate and the differences between two methods of analysis become more significant.

The evolution of the energy of the optical transitions upon Cr doping of TiO_2 is demonstrated in Fig. 10. The energy of the fundamental band gap E_g and that of the impurity band E_{dop} indicated in Fig. 10 were found from the analysis of the differential reflectance as a function of wavelength (from Fig. 8). Nanopowders with the chemical compositions falling within the range of 0–1.0 at.% Cr show two values of E_g. The higher one (E_{gI}) corresponds to the band gap energy of anatase while the lower one (E_{gII}) is that of rutile. The fundamental band gap of TiO_2 increases slightly with the chromium concentration. This may be accounted for by a modification of crystal structure. Incorporation of Cr^{3+} into TiO_2 lattice promotes the growth of rutile and causes a small decrease in the

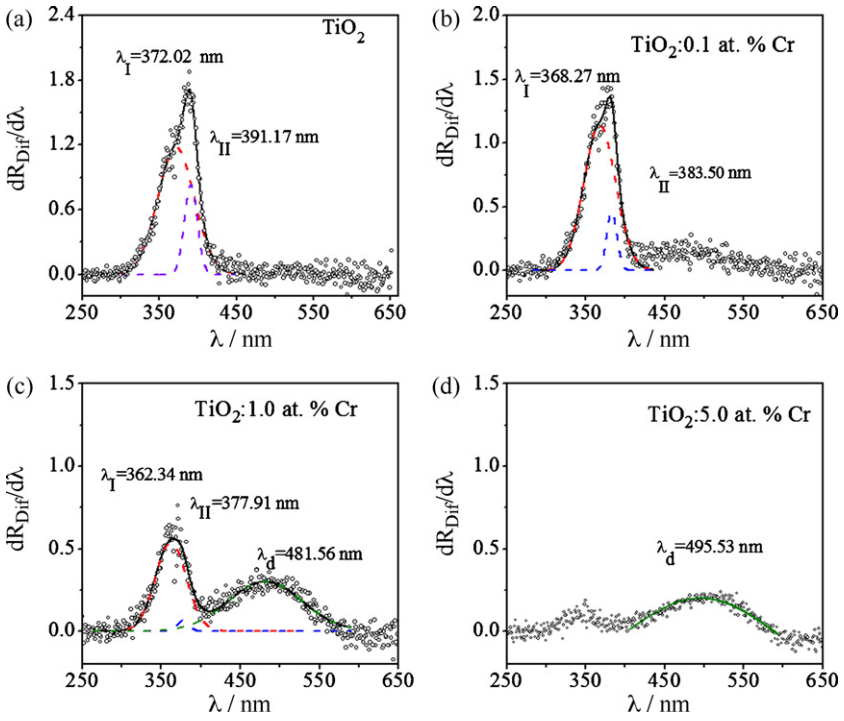

Fig. 8. Analysis of the optical transitions from reflectance spectra of TiO_2 and TiO_2:Cr nanopowders prepared by FSS; first derivative spectrum $dR_{Diff}/d\lambda$; λ_I, λ_{II} and λ_d represent wavelengths at which $dR_{Diff}/d\lambda$ attains the maximum.

size of the crystallographic cell (see Table 1). These two fundamental optical transitions are suppressed at the doping level exceeding 1 at.% Cr.

The band located at about 2.5–2.6 eV below the bottom of the conduction band of TiO_2 is related to chromium doping and that is why the energy E_{dop} of the optical transitions from this band to the conduction band of TiO_2 depends slightly upon the Cr content. This transition energy could be explained by excitation of an electron of Cr^{3+} impurity band located 1.0 eV above the VB into the CB of TiO_2.

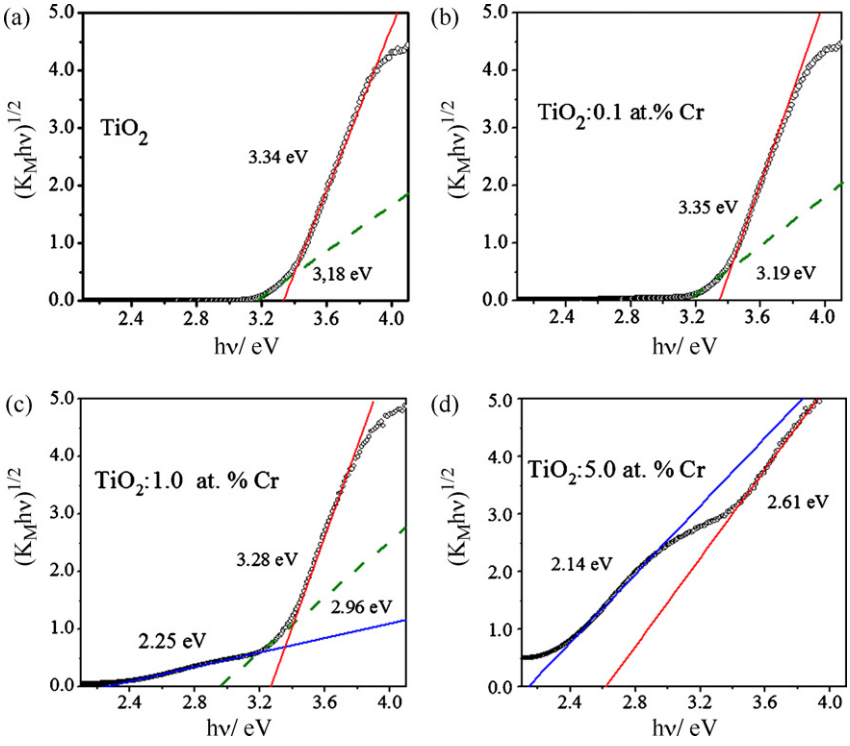

Fig. 9. Analysis of the optical transitions from transformed Kubelka–Munk spectra $(K_M h\nu)^{1/2}$ of TiO_2 and TiO_2:Cr nanopowders prepared by FSS; $h\nu$—photon energy, K_M–Kubelka–Munk function.

Table 3
Energies of optical transitions determined from two methods of analysis of the $R_{Diff}(\lambda)$ spectra.

at.%Cr	$dR_{Diff}/d\lambda$			Kubelka–Munk		
	E_{gI} (eV)	E_{gII} (eV)	E_{dop} (eV)	E_{gI} (eV)	E_{gII} (eV)	E_{dop}(eV)
0	3.33	3.17		3.34	3.18	
0.1	3.36	3.23		3.35	3.19	
1	3.42	3.38	2.57	3.28	2.96	2.25
5			2.50			2.14

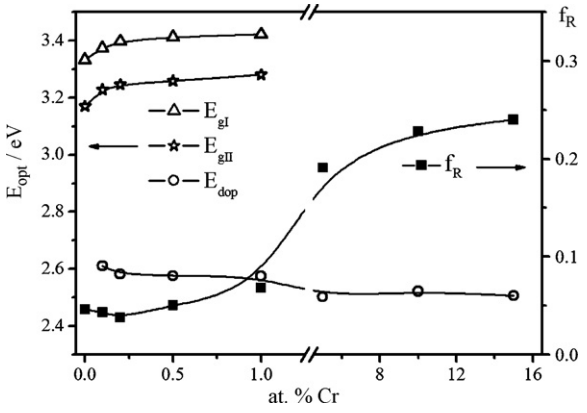

Fig. 10. Energy of the optical transitions E_{opt} as a function of Cr concentration in TiO_2 (left hand axis); E_{gI} and E_{gII} correspond to the fundamental band gap of anatase and rutile, respectively; E_{dop} is the energy of the transition from the band related to Cr impurity that is formed within the band gap of TiO_2. The rutile-to-anatase ratio f_R is given for comparison (right hand axis).

4. Conclusions

Nanopowders of TiO_2:Cr with the crystallite size within the range of 5–21 nm corresponding to the specific surface area from 48 m^2/g to 177 m^2/g were successfully obtained by FSS from precursors of titanium tetraisopropoxide and solution of chromium acetylacetonate in m-xylene. XRD and TEM analysis indicated that the observed decrease in grain and particle size was accompanied by an increased level of the amorphous background. It should be clarified in future investigation, if high Cr-doping lowers the degree of crystallinity, or if it is a pure size effect and results from the change in the surface–volume ratio. While both polymorphic phases of TiO_2, i.e., anatase and rutile were found, stabilization of rutile proceeded with an increased doping with chromium and rutile content increased significantly at about 15 at.% Cr. The binding energies determined from XPS indicate that chromium is present as Cr^{3+} in TiO_2:Cr nanopowders. The optical spectrophotometry over the UV and visible range of the light spectrum was used to determine the energy of the optical transitions from the valence band VB or impurity band to the conduction band CB of TiO_2 as a function of the concentration of chromium. Both Kubelka–Munk analysis and differential reflectance spectra were considered. The presence of the additional absorption within the visible range of the light spectrum at about 2.5–2.6 eV could be explained by excitation of an electron from Cr^{3+} impurity band, located above VB of TiO_2, into the CB of TiO_2. Such a strong modification of the absorption spectrum seemed to be a promising result as far as the photoelectrochemical and photocatalytic applications were considered.

Acknowledgement

The financial support of Polish Ministry of Science and Higher Education grant no. R15 019 02 is highly acknowledged.

References

[1] H.P. Maruska, A.K. Gosh, Sol. Energy Mater. 1 (1979) 237–247.
[2] G. Campet, J. Verniolle, J.P. Doumer, Mater. Res. Bull. 15 (1980) 1135–1141.
[3] K. Wilke, H.D. Breuer, J. Photochem. Photobiol. A: Chem. 121 (1999) 49–53.
[4] M. Radecka, K. Zakrzewska, M. Wierzbicka, A. Gorzkowska, S. Komornicki, Solid State Ionics 157 (2003) 379–386.
[5] M. Radecka, M. Rekas, A. Trenczek-Zajac, K. Zakrzewska, J. Power Sources 181 (2008) 46–55.
[6] J. Zhu, Z. Deng, F. Chen, J. Zhang, H. Chen, M. Anpo, J. Huang, L. Zhang, Catal. Appl. B: Environ. 62 (2006) 329–335.
[7] J.M. Herrmann, J. Disdier, P. Pichat, Chem. Phys. Lett. 108 (1984) 618–622.
[8] M. Radecka, M. Wierzbicka, S. Komornicki, M. Rekas, Physica B: Condensed Matter 348 (2004) 160–168.
[9] W. Choi, A. Termin, M.R. Hoffmann, J. Phys. Chem. 98 (1994) 13669–13679.
[10] Ch-Ch. Tsai, H. Teng, Appl. Surf. Sci. 254 (2008) 4912–4918.
[11] H. Yamashita, M. Honda, M. Harada, Y. Ichihashi, M. Anpo, T. Hirao, N. Itoh, N. Iwamoto, J. Phys. Chem. B 102 (1998) 10707–10711.
[12] Y. Wang, H. Cheng, Y. Hao, J. Ma, W. Li, S. Cai, Thin Solid Films 349 (1999) 120–125.
[13] X. Chen, S.S. Mao, Chem. Rev. 107 (2007) 2891–2959.
[14] K.K. Akurati, A. Vital, G. Fortunato, R. Hany, F. Nueesch, T. Graule, Solid State Sci. 9 (2007) 247–257.
[15] Z. Zhang, Ch-Ch. Wang, R. Zakaria, J.Y. Ying, J. Phys. Chem. B 102 (1998) 10871–10878.
[16] S. Karvinen, R.J. Lamminmäki, Solid State Sci. 5 (2003) 1159–1166.
[17] A. Di Paola, G. Marci, L. Palmisano, M. Schiavello, K. Uosaki, S. Ikeda, B. Ohtani, J. Phys. Chem. B 106 (2002) 637–645.
[18] D. Dvoranová, V. Berezová, M. Mazur, M.A. Malati, Appl.Catal. B: Environ. 37 (2002) 91–105.
[19] M. Anpo, M. Takeuchi, J. Catal. 216 (2003) 505–516.
[20] K.K. Akurati, A. Vital, J.-P. Dellemann, K. Michalow, T. Graule, D. Ferrim, A. Baiker, Appl. Catal. B: Environ. 79 (2008) 53–62.
[21] K.A. Michalow, A. Vital, A. Heel, T. Graule, F. Reifler, A. Ritter, K. Zakrzewska, M. Rekas, J. Adv. Oxidation Technol. 11 (2008) 56–64.
[22] R.D. Shannon, Acta Crystallogr. A32 (1976) 751–767.
[23] P. Kofstad, J. Less-Common Met. 13 (1967) 635–638.
[24] J. Nowotny, M. Radecka, M. Rekas, J. Phys. Chem. Solids 58 (1997) 927–937.
[25] R.M. Gibb, J.S. Anderson, J. Solid State Chem. 4 (1972) 379–390.
[26] O.W. Florke, C.W. Lee, J. Solid State Chem. 1 (1969) 445–446.
[27] C.W. Lee, Dt. Keram. Ges. 47 (1970) 169–175.
[28] K.T. Ranjit, B. Viswanathan, J. Photochem. Photobiol. A: Chem. 107 (1997) 215–221.
[29] J.L. Carpentier, A. Lebrun, F. Perdul, J. Phys. Chem. Solids 50 (1989) 145–151.
[30] M. Metikos-Hukovic, M. Ceraj-Ceric, Mat. Res. Bull. 23 (1988) 1535–1541.
[31] A. Bernasik, M. Radecka, M. Rekas, M. Sloma, Appl. Surf. Sci. 65/66 (1993) 240–245.
[32] M. Radecka, M. Rekas, Solid State Phenom. 39–40 (1994) 135–138.
[33] M. Radecka, M. Rekas, K. Zakrzewska, Opto-Electron. Rev. 2 (1994) 41–49.
[34] K. Zakrzewska, M. Radecka, M. Rekas, Thin Solid Films 310 (1997) 161–166.
[35] M. Radecka, A. Trenczek-Zajac, K. Zakrzewska, M. Rekas, J. Power Sources 173 (2008) 816–821.
[36] A.B. Murphy, Solar Energy Mater. Solar Cells 91 (2007) 1326–1337.
[37] K. Madhusudan Reddy, C.V. Gopal Reddy, S.V. Manorama, J.Solid State Chem. 158 (2001) 180–186.